Corrosion Science 190 (2021) 109607

Contents lists available at ScienceDirect

Corrosion Science

journal homepage: www.elsevier.com/locate/corsci

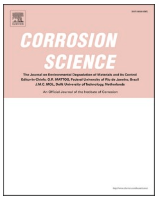

Corrosion performance of Ni-based structural alloys for applications in molten-salt based energy systems: Experiment & numerical validation

M. Lee [a,b], O. Muránsky [a,c,*], I. Karatchevtseva [a], H. Huang [d], K.J. Laws [b]

[a] Australian Science and Technology Organization (ANSTO), Sydney, NSW, Australia
[b] School of Materials Science & Engineering, UNSW, Sydney, Australia
[c] School of Mechanical and Manufacturing Engineering, UNSW, Sydney, Australia
[d] Shanghai Institute of Applied Physics (SINAP), Chinese Academy of Sciences, Shanghai, China

ARTICLE INFO

Keywords:
Molten salt corrosion
FLiNaK
Ni-Mo-Cr alloy
Oxide-dispersion-strengthened (ODS) alloy
Material mass loss

ABSTRACT

The molten salt corrosion performance of a Y_2O_3-strengthened Ni-Cr alloy (MA754®) designed for high temperature applications (> 750 °C) was compared to purpose-designed Ni-Mo-Cr molten-salt resistant alloys (GH3535, HASTELLOY-N®). The significant material mass loss of MA754® alloy is attributed to its higher Cr-content. However, Y_2O_3 dispersoids are shown to play only a minor role in the corrosion performance of this oxide-dispersion-strengthened (ODS) alloy. The current result, thus, points to the possibility for the development of low Cr-content ODS alloys that combines the high-temperature properties of ODS MA754® alloy with good molten salt corrosion resistance of well-established GH3535 and HASTELLOY-N® alloys.

1. Introduction

The production of CO_2 from fossil-fuel-based energy-generation systems is responsible for above 75 % of global greenhouse gas emissions and is therefore considered to be a major contributor to climate change [1]. While a number of low-emission energy sources currently exist, they each have their own challenges. For instance, renewable energy sources (e.g. wind, solar) suffer from low energy density, and significant intermittency due to weather conditions, while baseload low-emission sources such as nuclear-based systems struggle with public acceptance. The development of molten-salt-based energy-generation and energy-storage systems promises to alleviate at least some of these challenges by taking advantage of the excellent thermo-physical properties of molten salts. In particular, their high boiling point and low vapour pressure over a wide range of working temperatures is of interest, as they allow for low-pressure systems to be designed, which are inherently safe against any explosion-like accidents [2]. Furthermore, their high thermal diffusivity, relatively low viscosity, non-flammability and high chemical stability makes molten-salt-based systems an attractive alternative to conventional technologies [3].

The potential of molten salt reactor (MSR) systems for civilian applications was first recognised in the 1950s during the Aircraft Nuclear Propulsion (ANP) program [4]. Oak Ridge National Laboratory (ORNL) ran the Molten Salt Reactor Experiment (MSRE) throughout the 1960s, demonstrating the viability of MSR technology utilizing fluoride molten salts [4]. Interest into MSR systems was renewed decades later following the formation of the Generation IV International Forum (GIF) in 2001 [5]. Recently, government agencies have been joined by a number of start-up companies (e.g. Terrestrial Energy, Terra Power, Moltex) that pursue the near-future deployment of commercially viable fluoride-and-chloride-based MSR systems. Furthermore, the renewable energy industry has built upon this decades' long effort by developing molten-salt-based thermal energy storage (TES) to combat the non-dispatchable nature of renewable energy sources [6]. Proposed next generation TES systems are being designed to utilise fluoride or chloride salts (similar to MSR systems) due to their higher operation temperatures in contrast to nitride and carbonite salts [7].

The primary challenge of using fluoride and chloride molten salts as an energy-transfer and energy-storage fluid is their severe corrosivity to most common structural materials [8]. Note, that candidate structural materials are expected to withstand a combination of extreme in service environmental conditions such as high temperature, molten salt corrosion and high neutron flux in the case of nuclear-based systems. It was recognised during the MSRE that Ni-Mo-Cr alloys provided the highest degree of corrosion resistance, which led to the development of HASTELLOY-N® (USA) [9], and more recently GH3535 (China) [10] and

---

[*] Corresponding author at: Australian Science and Technology Organization (ANSTO), Sydney, NSW, Australia.
E-mail address: ondrej.muransky@ansto.gov.au (O. Muránsky).

https://doi.org/10.1016/j.corsci.2021.109607
Received 17 November 2020; Received in revised form 6 May 2021; Accepted 1 June 2021

Table 1
Chemical composition (mol%) of tested alloys.

Element	Inconel MA754®	GH3535	HASTELLOY-N®
Ni	Bal.	Bal.	Bal.
Mo	–	16	16.5
Cr	20	7	7.4
Fe	1	4	3.5
Si	–	1	1
Mn	–	0.8	0.8
Y	0.6	–	–
V	–	0.5	0.5
W	–	0.5	0.5
Cu	–	0.35	0.35
Ti	0.5	0.25	0.25
Al	0.3	0.25	0.25
C	0.05	0.06	0.06
Co	–	0.02	0.02

MONICR® (EU) [11]. However, the inadequate high-temperature (> 750 °C) performance of these Ni-Mo-Cr alloys have prompted interest into other Ni-based alloys, such as the oxide-dispersion-strengthened (ODS) Ni-Cr alloys, which is known to maintain the mechanical properties (high temperature creep and creep-fatigue) at temperatures of up to 1000 °C [12]. Hence, we aim to compare the corrosion behaviour of an Y_2O_3-strenghtend MA754® alloy with the purpose-designed molten-salt alloys.

The present work compares the corrosion performance of MA754® ODS alloy with HASTELLOY-N®, and GH3535 alloys in FLiNaK molten salt at 750 °C for 300 h. The extent of corrosion is evaluated from the measured material mass loss as a result of exposure to molten salt. The impact of molten salt corrosion on the microstructure of tested alloys is then examined using combined Energy-Dispersive Spectroscopy (EDS) and Electron Back-Scatter Diffraction (EBSD) analysis. Finally, the experimental mass loss results are compared with numerical predictions based on the time-dependent depletion of alloying elements from the corrosion-affected surface layer. We show that the Y_2O_3-strengthened alloy MA754® has inferior corrosion resistance compared to both GH3535 and HASTELLOY-N®, which is attributed to the higher Cr content of the alloy composition. Furthermore, it is shown that Y_2O_3 dispersions have a limited effect on the corrosion performance of the alloy. Hence, this research points to possibilities for the development of corrosion resistance dispersion-strengthened Ni-Mo-Cr alloys for applications at temperatures above 750 °C.

2. Experimental

2.1. Material

The chemical composition of the studied alloys are given in Table 1, while their as-received microstructures are compared via EBSD orientation maps in Fig. 1. This reveals that the microstructure of GH3535 (Fig. 1b) and HASTELLOY-N® (Fig. 1c) are similar, both containing large equiaxial grains (> 50 μm) with a significant number of annealing twins and approximately 1.25 vol.% of $M_6[C,Si]$ carbides, where M = Mo, Cr, Fe, Ni, and Mn [13]. This stands to reason as GH3535 is equivalent to the ORNL-developed HASTELLOY-N®, designed to be used as a structural material in MSR systems. Both alloys were provided by the Shanghai Institute of Applied Physics (SINAP, China) as plates in the solution-annealed condition. Inconel alloy MA754® is an oxide-dispersion-strengthened, Ni-Cr alloy produced by mechanical alloying followed by hot-rolling and solution-annealing. Unlike GH3535 and HASTELLOY-N®, MA754® alloy was not developed with molten salt corrosion resistance in mind. However, the alloy utilises a dispersion

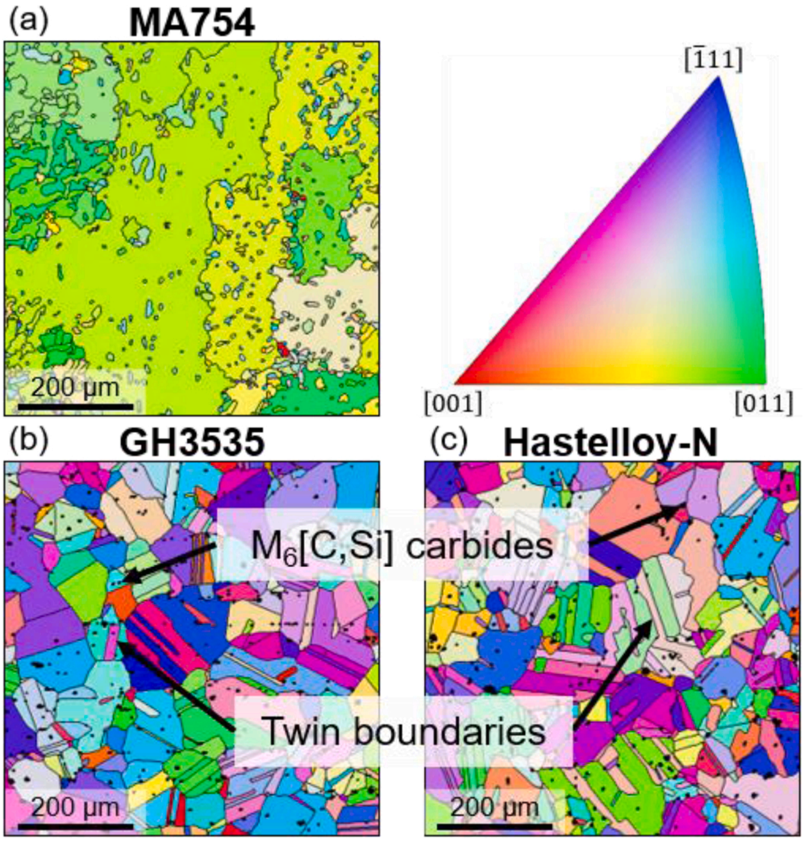

Fig. 1. EBSD orientation maps taken at 100× magnification of as-received microstructure of: (a) Inconel MA754®, (b) GH3535 and (c) HASTELLOY-N®. Inconel MA754® exhibits a mixture of large equiaxial (>50 μm) and fine elongated (<10 μm) grains while Gh3535 and HASTELLOY-N exhibit mostly large equiaxed (>50 μm) grains.

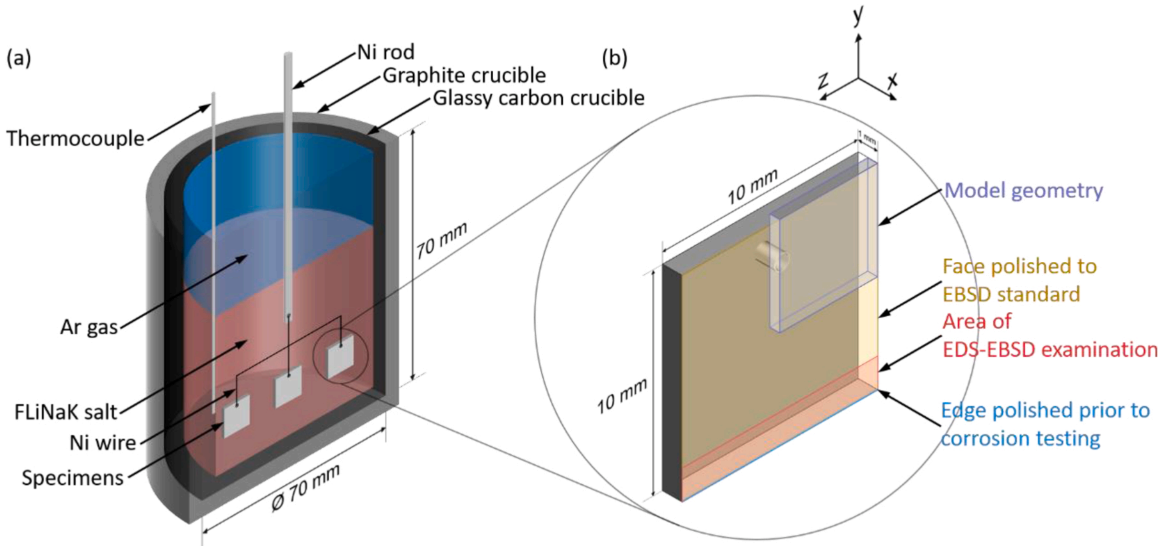

Fig. 2. Schematic diagram of the molten salt corrosion testing setup and alloy specimen. Alloy specimen shows the size of the model geometry employed in the numerical model simulations, regions subjected to different polishing treatments and areas undergone EDS-EBSD examination.

Table 2
Parameters used to set up numerical model geometry and boundary conditions.

Dimension	Length (mm)	Number of divisions	Boundary conditions
x	0.5	500	Symmetry boundary condition Surface film boundary condition (sink temperature = 0)
y	5	5	Symmetry boundary condition
z	5	5	Symmetry boundary condition
Total number of elements: 12500			
Total number of increments: 300			

Table 3
Diffusion coefficients of Cr, Mn and Si used in numerical model predictions.

Element	Diffusion coefficient (D) (cm^2/s)	Maximal diffusion coefficient (D_0) (cm^2/s)	Activation energy (E_A) (J/mol)	Ref.
Al	2.1451×10^{-13}	1.1	−248948	[44]
Cr	5.7775×10^{-11}	0.03	−170707	[45]
Mn	6.2759×10^{-11}	1.02	−200000	[46]
Si	9.9129×10^{-14}	1.5	−258153	[47]
Ti	9.2293×10^{-14}	0.0027	−205000	[48]

of nano-sized Y_2O_3 particles to provide high-temperature strength as well as creep and creep-fatigue resistance to the Ni-Cr matrix at temperatures of up to 1000 °C [12]. Fig. 1a shows that MA754® has a significantly different bi-modal microstructure consisting of large irregular-shaped grains (> 50 μm) and fine elongated grains (< 10 μm). Note that while Y_2O_3 particles dispersed across the microstructure are not visible in the present EBSD orientation map, however, they have been studied extensively using other experimental techniques – see Refs. [14–17].

2.2. Molten salt corrosion testing

Molten salt corrosion testing was performed at ANSTO using in-house developed apparatus (Fig. 2a) at 750 °C for 300 h in FLiNaK molten salt. Since the chemical composition of GH3535 and HASTELLOY-N® are virtually identical (Table 1), they were tested simultaneously, while MA754® was tested separately using the identical experimental set-up to avoid dissimilar material corrosion (galvanic corrosion). FLiNaK molten salt mixture (42.0–46.5–11.5 mol.% - eutectic composition) was prepared from commercially available KF (60239), LiF (62497), NaF (201154) salts supplied by Sigma-Aldrich (≥ 99.0 wt. % purity). Salt mixing was done in a glove box under nitrogen atmosphere to minimise the amount of moisture in the mixture. The concentration of pre-existing impurities provided by supplier are given in Appendix A1. Note that no additional purification of the salt was performed in order to investigate the effect of commonly present molten salt impurities [18,19]. A glassy carbon crucible (70 mm height, 70 mm outer diameter, 250 mL capacity) was filled with 200 g of the prepared FLiNaK molten salt in a glove box before being transferred to pre-heated (150 °C) tube furnace. A K-type thermocouple in a nickel casing was placed in the crucible to allow for temperature control throughout the experiment as shown schematically in Fig. 2a. To minimise the amount of moisture and volatile impurities in the molten salt, the temperature of the furnace was slowly raised to 750 °C at a rate of 2 °C/min under vacuum. Two holding periods at 200 °C and 500 °C were used to degas the system until a stable vacuum (0.6 mbar) was re-established. Following the salt-preconditioning (approximately 48 h in total), over-pressured argon gas (99.997 wt. % purity) at 34 kPa was used to purge the furnace. The argon gas flow was maintained throughout the experiment to prevent air from entering the furnace. Only then were three specimens (10 × 10 × 1 mm) of each alloy lowered into the crucible while being attached to the specimen holder using nickel wires as shown in Fig. 2a. Note that one edge of each specimen, opposite to the holding wire was progressively polished prior to the molten salt testing, this area was later examined to investigate the effect of molten salt corrosion on the microstructure (see Fig. 2b, and section 2.3). Since GH3535 and HASTELLOY-N® were tested simultaneously, six specimens (three of each alloy) were in the crucible at the same time. When testing MA754®, only three specimens of the alloy were in the crucible during testing. Note that throughout the entire experiment, all specimens were fully submerged in the FLiNaK molten salt whilst ensuring no physical contact was made between the individual specimens or with the crucible walls. Following molten salt testing, specimens were removed from the furnace and the furnace was allowed to cool to room temperature. Residual solidified salt on the specimens' surfaces were dissolved using aqueous $Al(NO_3)_3$ solution (20 wt.%) so that the material mass loss as a result of exposure to the molten salt could be determined.

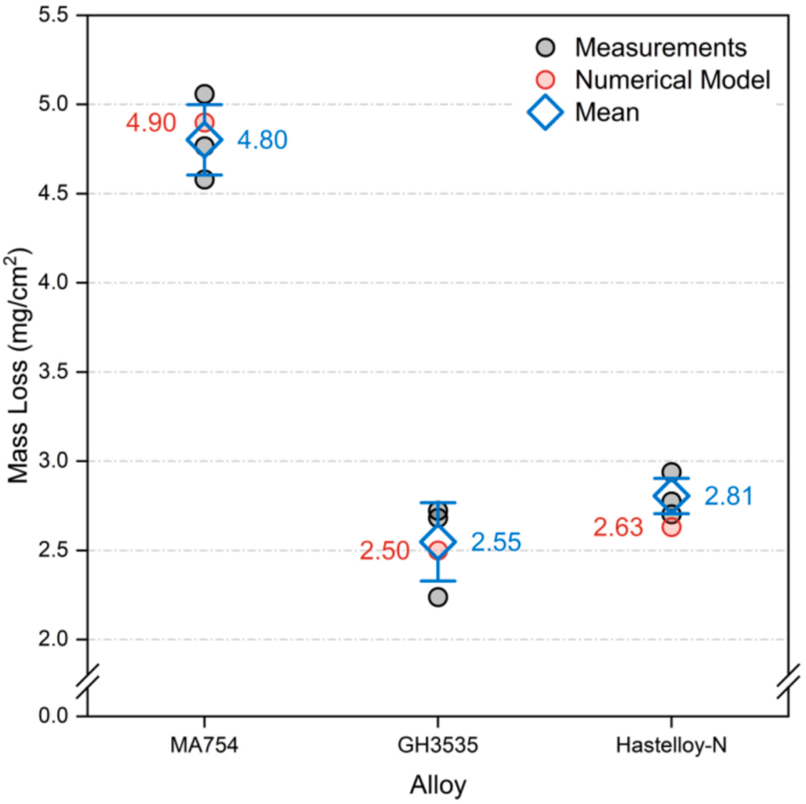

Fig. 3. Mass loss comparison between experimental data obtained from molten salt corrosion testing with numerical model predictions, normalised with respect to the specimen surface area. Individual measurements are represented black symbols, mean mass loss is represented by blue symbols and numerical model prediction is represented by red symbols. Error bars represent one standard deviation (For interpretation of the references to colour in this figure legend, the reader is referred to the web version of this article).

2.3. *Microstructural characterisation*

A Zeiss UltraPlus Scanning Electron Microscope (SEM) equipped with both EBSD and EDS detectors was employed to characterise the microstructure of the studied alloys in both as-received and post-corrosion conditions. Following the molten salt testing, one face (10 × 10 mm, Fig. 2b) of each specimen was progressively polished to an EBSD standard to allow for microstructure examination of the corrosion-affected surface layer. To examine the effect of molten salt corrosion on the alloys' microstructure and chemical composition, EBSD-EDS maps were collected simultaneously at various magnifications (100x, 500x and 2000x) corresponding to different pixel separation distances (1000 nm, 150 nm, and 20 nm – spatial resolution). The EBSD-EDS maps of post-corrosion specimens were collected close to the pre-polished edge opposite the specimen's point of attachment to the nickel rod during corrosion testing (Fig. 2b). All collected maps were analysed using MATLAB® [20], employing functionality of the MTEX Toolbox [21].

2.4. *Numerical validation*

ABAQUS® finite element package [22] was employed to predict the depletion of fluoride-forming alloying elements (Al, Cr, Mn, Si and Ti) leading to material mass loss as a result of molten salt corrosion. Each alloy was inputted into the ABAQUS material database as a new material with their respective alloy compositions and diffusion constants. The geometry of the developed 3D model containing 12500 heat transfer-type elements is shown in Fig. 2b. Note that a quarter-model with defined symmetry planes (boundary conditions listed in Table 2) was utilised to decrease computational time. After mesh sensitivity analysis, a mesh size of x =1 μm, y = 1 mm, z = 1 mm was chosen as a balance between the model accuracy and model size (computation time). The model was iterated over 300 increments to approximate the corrosion behaviour of each specimen over 300 h.

The mass diffusion of the alloying elements leading to mass loss was simulated using the "Surface Film" boundary condition with the sink temperature set at 0. This boundary condition was chosen as the concentration of the depleted alloying elements were assumed to be at 0 wt.% at the surface of the specimen. Note that at high temperatures, mass diffusion is dominated by bulk diffusion [23], which is known to be well predicted by the Arrhenius equation:

$$D = D_0 e^{-\frac{E_A}{RT}}, \tag{1}$$

where D is the diffusion coefficient, D_0 is maximal diffusion coefficient, E_A is activation energy, R is universal gas constant (8.3145 J/mol/K), T is temperature during corrosion testing (1023.15 K). Importantly, the diffusion coefficients of fluoride-forming alloying elements (Al, Cr, Mn, Si and Ti) in Ni matrix were obtained from literature and are tabulated in Table 3. The output concentration gradient in the x-direction (Fig. 2b) was then analysed and the mass loss for each alloying element was determined. The overall mass loss was calculated by converting the ABAQUS predicted concentration gradient into mass loss per distance [mg/μm] and multiplying it by the volume of the specimen (10 × 10 × 1 mm). Finally, the overall mass loss was normalised with respect to the surface area of the model geometry to obtain a mass loss per surface area [mg/cm^2] to facilitate direct comparisons between experimental measurements and numerical predictions. It needs to be emphasised that the current model does not contain any microstructural information (e.g. grain size, dislocations, second-phase particles) which have been shown to meaningfully affect molten salt corrosion of structural alloys as suggested in Refs. [24–27]. The present simulations should, therefore, be taken only as an approximation of the corrosion behaviour of the alloy. However, the development of reliable numerical predictions is of technological importance when it comes to operating of any future molten-salt-based energy system.

3. Results and discussion

The recorded mass loss of tested alloys are compared in Fig. 3. Note

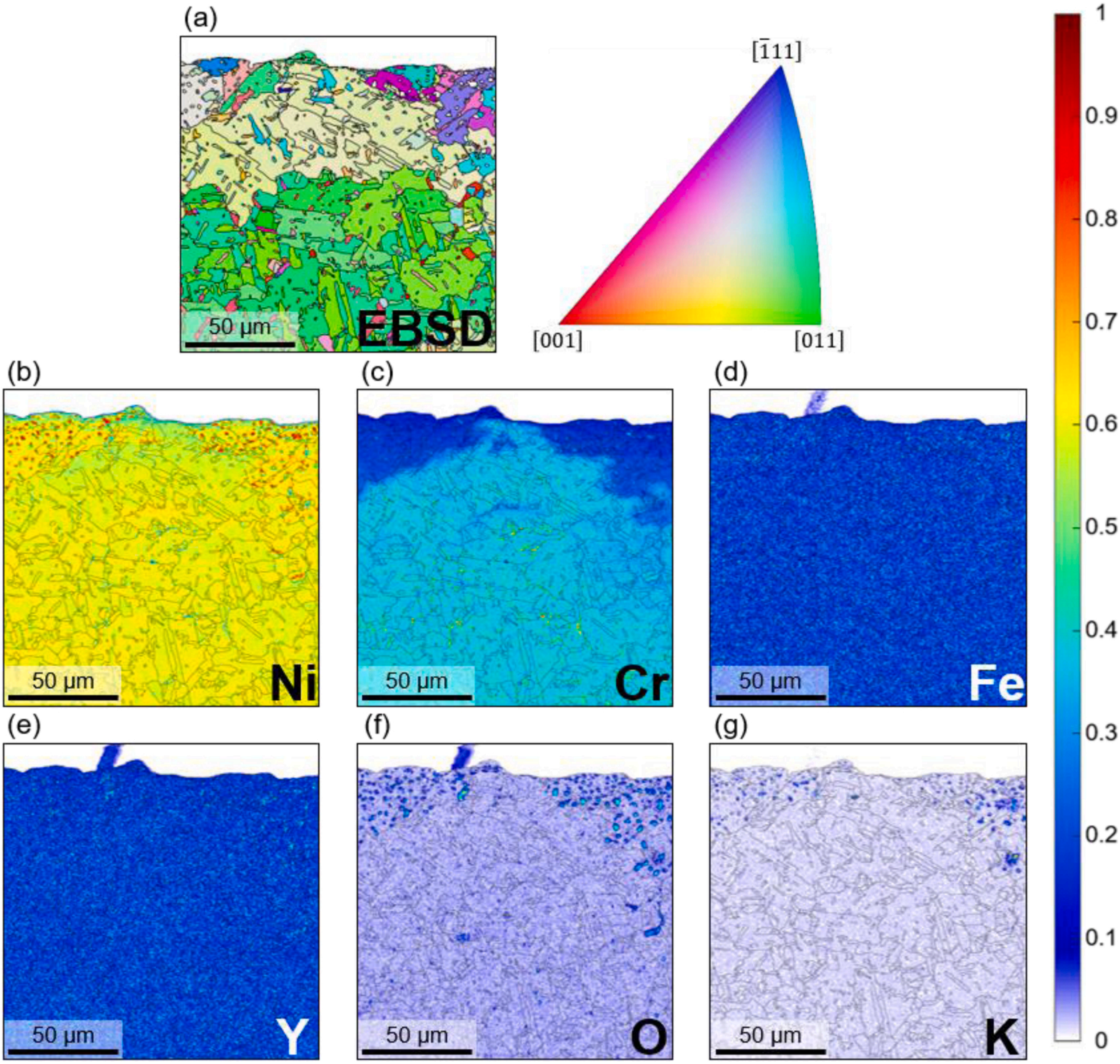

Fig. 4. EBSD-EDS maps taken at 500× magnification of Inconel MA754® following molten salt corrosion testing at 750 °C for 300 h, showing: (a) EBSD map; (b) Ni EDS map; (c) Cr EDS map; (d) Fe EDS map; (e) Y EDS MAP; (f) O EDS map and (g) K EDS map. Figures (b)-(g) are min-max normalised between 0-1 (see scale bar).

that the error bar represents the standard deviation of the mass loss measurements of three individual alloy specimens – see experimental setup in Fig. 2a. It is evident from the present results that ODS MA754® alloy exhibited significantly more mass loss compared to GH3535 and HASTELLOY-N® alloys. On the other hand, similar corrosion performance of GH3535 and HASTELLOY-N® is expected due to their similar chemical (Table 1) and microstructural characteristics – this agrees with our previous results in Ref. [28]. In what follows, we first investigate the effect of molten salt corrosion on the microstructure of the studied alloys using EBSD-EDS examination of the post-corrosion microstructure (section 3.1) and then we discuss the diffusion-based finite element model predictions – these are compared to overall material mass loss and experimental EDS maps (section 3.2).

3.1. Molten salt corrosion mechanisms

The EBSD-EDS observations of post-corrosion specimens at the corrosion-affected surface layer of the studied alloys are shown in Fig. 4 (MA754®), 5 (GH3535) and 6 (HASTELLOY-N®). While EBSD orientation maps suggest that there are no significant changes in the microstructure of the studied alloys during the molten salt testing, signs of recrystallization can be seen in the corrosion-affected layer of GH3535 (see the fine-grained microstructure on the alloy surface in Fig. 5a). No recrystallization of the corrosion-affected layer (Fig. 6a) was observed in HASTELLOY-N® despite its very similar chemical (Table 1) and microstructural characteristics (Fig. 1) which suggests its greater thermal stability. Upon examination of the EDS compositional maps, it becomes apparent that Cr is being depleted from the exposed surface in all tested alloys, but to a far greater extent in ODS MA754® alloy. The depletion of Cr in MA754® alloy is accompanied by a minor depletion of Al and Ti and the formation of Ni and K rich oxides – see Fig. 4b-g. While no such formation of oxides is observed in GH3535 and HASTELLOY-N® alloys, they show depletion of other alloying elements such as Si, Mn, and to a lesser degree, Mo. Note that similar to other authors, a limited enrichment of the corrosion-affected layer of these Ni-Mo-Cr alloys by Ni and Fe was observed. However, this was found to have a minor effect on the

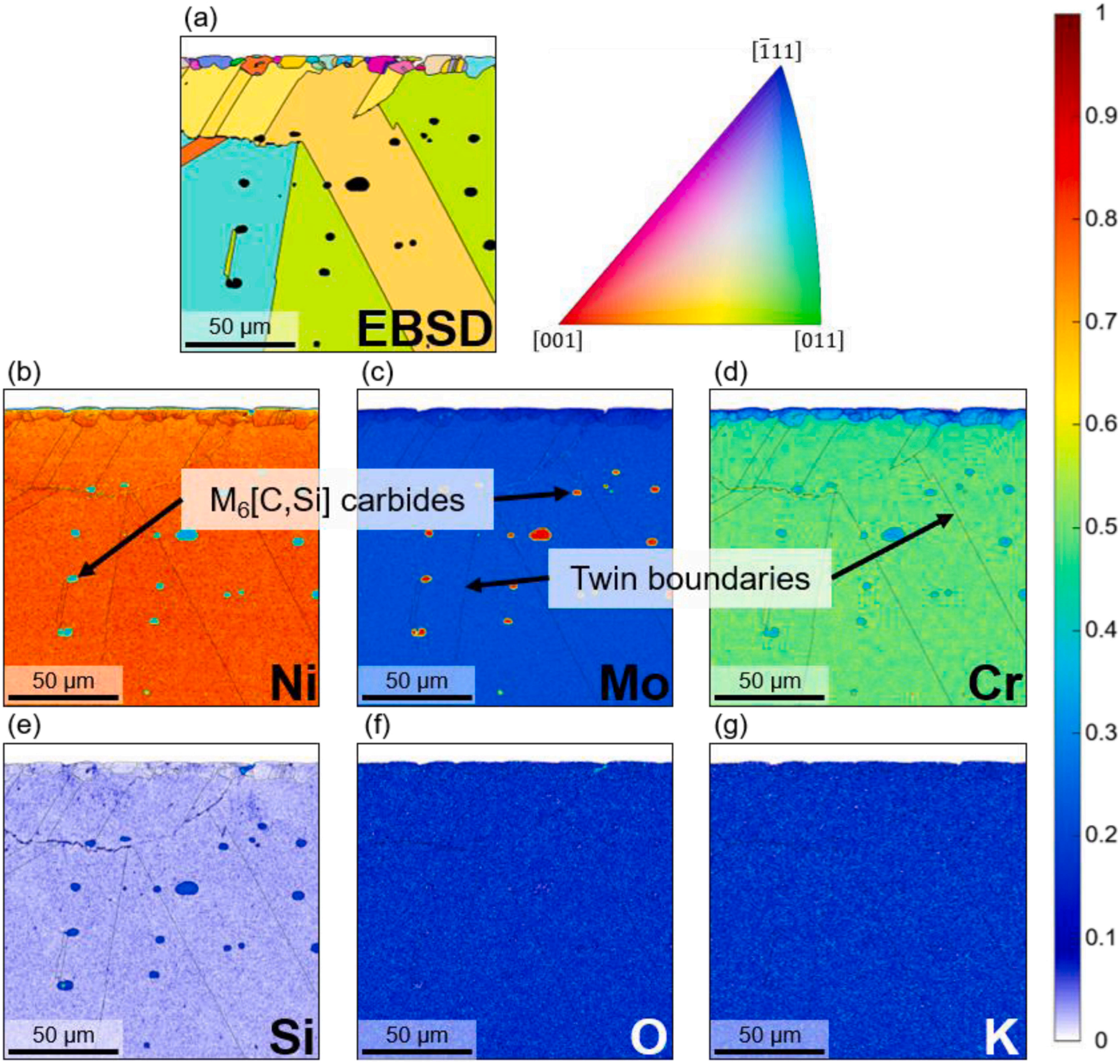

Fig. 5. EBSD-EDS maps taken at 500× magnification of GH3535 following molten salt corrosion tests at 750 °C for 300 h, showing: (a) EBSD map; (b) Ni EDS map; (c) Cr EDS map; (d) Fe EDS map; (e) (Y) EDS MAP; (f) O EDS map and (g) K EDS map. Figures (b)-(g) are min-max normalised between 0-1 (see scale bar).

overall material mass loss [28]. In what follows, we provide insights into the underlying processes leading to the depletion of the various alloying elements, resulting in the observed material mass loss shown in Fig. 3.

In general, the molten salt corrosion is governed by the Gibbs free energy of formation (ΔG_f^o) of potential corrosion products between the alloy and molten salt constituents (LiF, NaF, KF) – see the Gibbs free energies of formation of potential corrosion products in Appendix A2. Assuming pure molten FLiNaK salt, no significant corrosion should take place because the fluorides of salt constituents are thermodynamically more stable than any potential fluoride of alloying elements [29]. However, it has been shown that commonly present impurities such as moisture, and metallic fluorides leads to an impurity-assisted thermodynamically-driven corrosion mechanism [30] – discussed in detail below. Note that the corrosion process is further affected by the diffusion rate of reactive alloying elements to the alloy-salt interface and the rate at which formed corrosion products dissolve into the molten salt [31].

A basic fluorination reaction between a metallic element of an alloy and a salt constituent to form a metal fluoride can be described by the following reaction [30]:

$$xMe(s) + yMF(l) \rightarrow Me_xF_y(l) + yM(l) \tag{2}$$

where *Me* is an alloying element (Cr, Mn, Si etc.) and *MF* is a constituent salt. Unlike oxides in oxygen-rich environments, the formed fluoride corrosion products (Me_xF_y) do not act as a protective layer as they are readily dissolved into the molten salt mixture, thus exposing underlying material [32], while they can also act as an oxidizer for other alloying elements. As mentioned above, in theoretically pure FLiNaK molten salt, no corrosion would take place as ΔG_f^o of formation of salt constituents (LiF, NaF, KF) are more negative than any of the potential corrosion products – see Appendix A2. However, small amounts of molten salt impurities (e.g. H_2O, SO_4^{2-}, Me_xF_y) will significantly alter the thermodynamic equilibrium of the system leading to new pathways for reactions between the constituent salts and the alloy to take place. Hence, in practice, impurity-assisted thermodynamically-driven corrosion is the primary driving force of alloy corrosion in molten salts. In what follows,

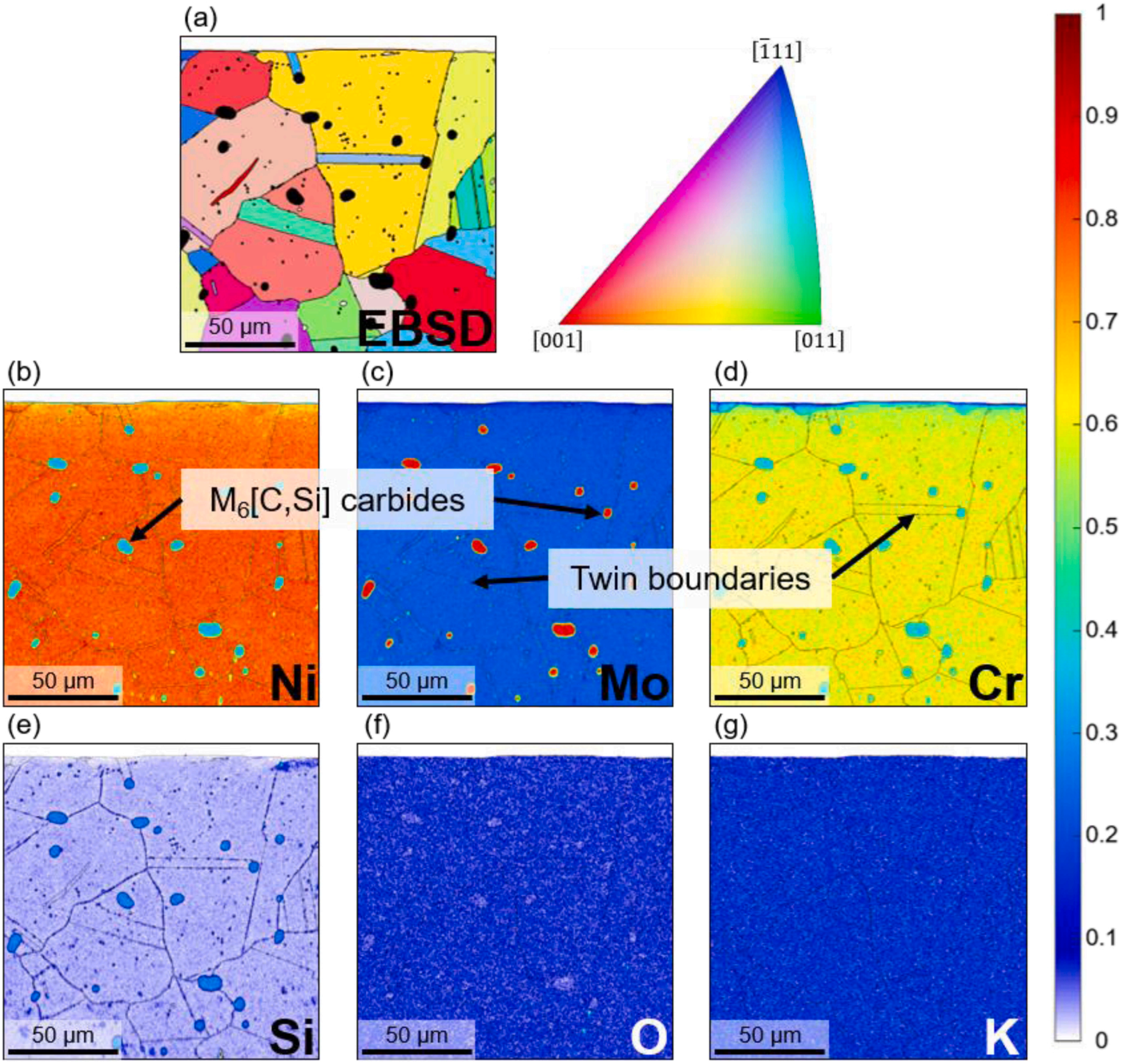

Fig. 6. EBSD-EDS maps taken at 500× magnification of HASTELLOY-N® following molten salt corrosion tests at 750 °C for 300 h, showing: (a) EBSD map; (b) Ni EDS map; (c) Mo EDS map; (d) Cr EDS map; (e) Si EDS MAP; (f) O EDS map and (g) K EDS map. Figures (b)-(g) are min-max normalised between 0-1 (see scale bar).

we discuss the effects of the most common molten salt impurities on the formation of corrosion products.

Moisture is known to be the most deleterious impurity found in molten salts due to its ability to react with constituent salts to form highly corrosive HF [19,33], which will then react with alloying elements, leaching them from the alloy and into the molten salt [34]:

$$MF(l)+H_2O(l)\rightarrow MOH(l)+HF(g,\ l) \tag{3}$$

$$2MF(l)+H_2O(l)\rightarrow M_2O(l)+2HF(g,\ l) \tag{4}$$

$$xM\ e(s)+yHF(\ l)\rightarrow Me_xF_y(l)+\frac{y}{2}H_2(g) \tag{5}$$

These reactions will continuously deplete specific alloying elements from the corrosion-affected near-surface layer leading to the formation of vacancies which coalesce to form voids near the alloy-salt interface [30]. In addition, the presence of metallic fluoride impurities (Me_xF_y) allows thermodynamically favourable substitution redox reactions to take place with alloying elements. Note that Me_xF_y compounds can be present in the molten salt either as initial impurities or as corrosion products (Eq. (5)). These metallic fluorides can then act as oxidizers of other metals, for examples NiF_2 oxidizes Cr through a following reaction [34]:

$$Cr(s)+NiF_2(l)\rightarrow CrF_2(l)+Ni(s) \tag{6}$$

$$Fe(s)+NiF_2(l)\rightarrow FeF_2(l)+Fe(s) \tag{7}$$

Pavlík at el. [35] studied the effect of the addition of CrF_3, FeF_2, FeF_3, and NiF_2 in FLiNaK on the molten salt corrosion of Inconel 800H clearly showing the negative effect of metallic flourides on corrosion behaviour of the alloy. Since, the Ni^{2+} and Fe^{2+} ions are reduced to atomic Ni and Fe as shown in Eq. (6,7) they can also diffuse and deposit into the vacancies created by the depletion of alloying elements leading to the observed Ni and Fe enrichment of the corrosion-affected region. As discussed by other authors in Refs. [26,28,36,35], this mechanism has negligible effect on the recorded material mass loss. Fig. 3 shows that the depletion of alloying elements leading to material mass loss clearly

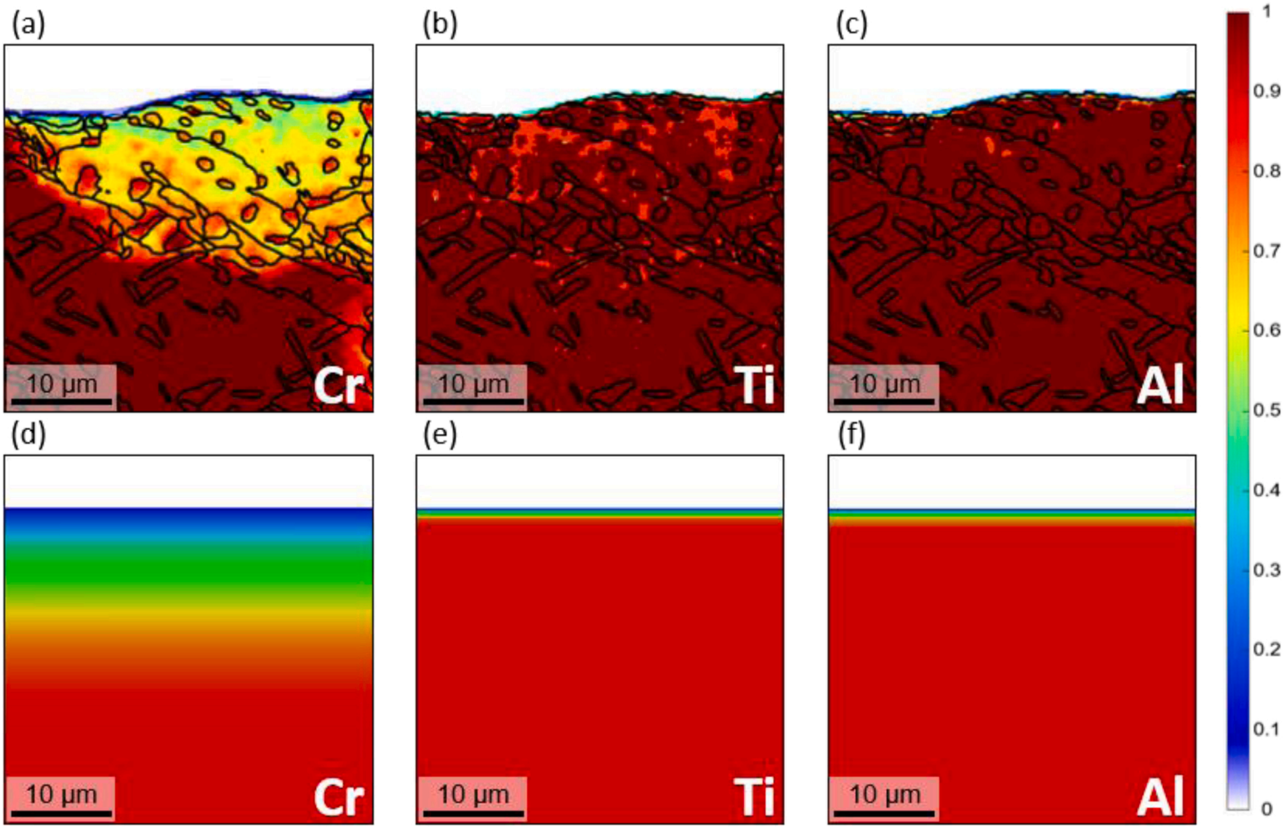

Fig. 7. EDS maps and modelled corrosion profiles taken at 2000× magnification of Inconel MA754® following molten salt corrosion tests at 750 °C for 300 h, showing (a) Cr EDS map; (b) Ti EDS map; (c) Al EDS map; (d) Cr modelled corrosion profile; (e) Ti modelled corrosion profile and (f) Al modelled corrosion profile. Figures (a)-(f) are min-max normalised between 0-1 (see scale bar).

outweighs the mass gained due to the enrichment of the corrosion-affected layer by Ni and Fe. However, the enrichment effect is expected to be more pronounced in a molten salt loop containing warmer and cooler regions, resulting in temperature-gradient-driven corrosion behaviour [30]. Furthermore, Cr, Mn and Si are known to react with dissolved SO_4^{2-} ions present in the molten salt, enhancing depletion of reactive alloying elements via the formation of oxides [18, 37].

$$2Cr(s) + SO_4{}^{2-}(l) \rightarrow Cr_2O_3(s) + S(l) + O^{2-}(l) \tag{8}$$

$$2Mn(s) + SO_4{}^{2-}(l) \rightarrow Mn_2O_3(s) + S(l) + O^{2-}(l) \tag{9}$$

$$Si(s) + SO_4{}^{2-}(l) \rightarrow SiO_2(s) + S(l) + 2O^{2-}(l) \tag{10}$$

It is clear from Gibbs free energies of formation of these reactions (Appendix A2), the potential of Mo fluoride (MoF_3, MoF_4, MoF_6) formation is thermodynamically unfavoured. Hence, the unexpected depletion of Mo from the corrosion-affected surface layer observed in both Ni-Mo-Cr alloys (Figs. 5 and 6) cannot be attributed to the aforementioned reactions. Instead, depletion of Mo is likely caused by the formation of Mo oxides from reacting with moisture and dissolved O^{2-} impurities present within the molten salt [38]:

$$Mo(s) + H_2O(l) \rightarrow MoO(l) + H_2(g) \tag{11}$$

$$Mo(s) + O^{2-}(l) \rightarrow MoO(l) + e^- \tag{12}$$

In addition to the aforementioned pathways, MA754® suffers from enhanced corrosion compared to GH3535 and HASTELLOY-N® partially due to the presence of Y_2O_3 dispersoids. Firstly, the accumulation of F in vacancies combined with the depletion of Y at the corrosion-affected surface layer suggests that Y_2O_3 particles undergo fluorination reactions with constituent salts to form fluorides [39]:

$$Y_2O_3(s) + 6LiF(l) \rightarrow 2YF_3(l) + 3Li_2O(s) \tag{13}$$

$$Y_2O_3(s) + 6NaF(l) \rightarrow 2YF_3(l) + 3Na_2O(s) \tag{14}$$

$$Y_2O_3(s) + 6KF(l) \rightarrow 2YF_3(l) + 3K_2O(s) \tag{15}$$

Furthermore, as corrosion occurs, O present within the alloy at the corrosion-affected surface layer diffuses out of the alloy and into the molten salt, increasing the concentration of O^{2-} impurities in the molten salt. Certain alloying elements, namely Cr, are then preferentially oxidised, leading to an increase in oxide formation [40]:

$$2Cr(s) + 3O^{2-}(l) \rightarrow Cr_2O_3(s) \tag{16}$$

3.2. Numerical prediction of depletion of alloying elements and overall material mass loss

A diffusion-based finite element model (ABAQUS) described in section 2.4 was employed to predict the depletion of alloying elements and resultant mass loss. The model considers the depletion of Al, Cr, Mn, Si and Ti as the Gibbs free energies of formation ($\Delta G_f{}^o$) of their fluoride corrosion products are relatively low (Appendix A2). Hence, they are likely to form during exposure to FLiNaK molten salt, thus contributing to the observed material mass loss. It should be noted that Mo was not considered as a depleting alloying element in the model, despite experimental data showing minor depletion of Mo via formation of oxides, rather than fluorides.

In Figs. 7–9we present a one-to-one comparison between the predicted depletion of considered alloying elements with corresponding experimental composition maps. Because the developed model does not contain any microstructural information (grain size, grain orientation,

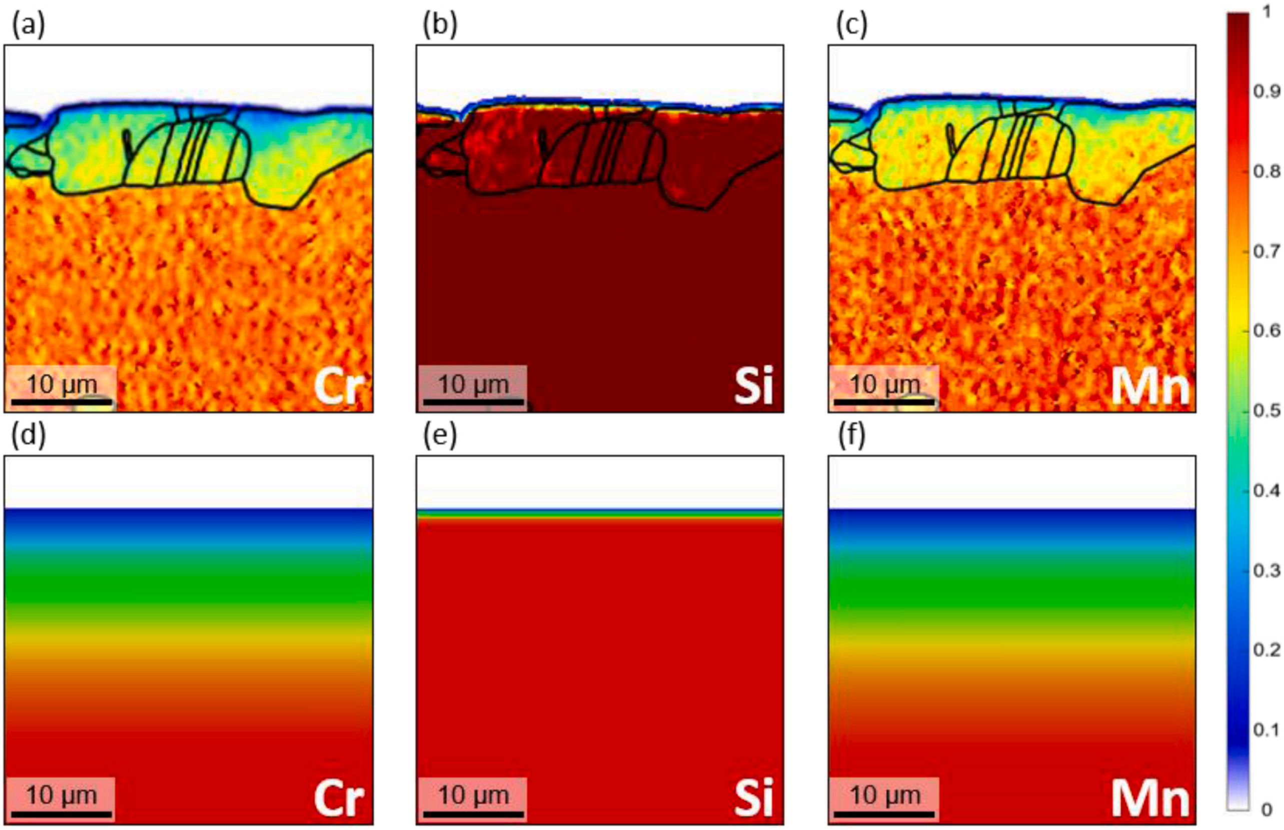

Fig. 8. EDS maps and modelled corrosion profiles taken at 2000× magnification of GH3535 following molten salt corrosion tests at 750 °C for 300 h, showing (a) Cr EDS map; (b) Mn EDS map; (c) Si EDS map; (d) Cr modelled corrosion profile; (e) Mn modelled corrosion profile and (f) Si modelled corrosion profile. Figures (a)-(f) are min-max normalised between 0-1 (see scale bar).

dislocations, second-phase particles, etc.) it is difficult to assess the model accuracy based on these one-to-one comparisons. Nevertheless, the developed model provides a reasonable estimate of the expected depth of the corrosion-affected layer and depletion of individual alloying elements.

In what follows, we focus on the overall prediction of molten salt corrosion behaviour of the tested alloys. It is clear from Fig. 3 showing mass loss for different alloys that there is good agreement between the numerical predictions and experimental measurements with a difference of less than 5%. These results suggest that a diffusion-based model captures the reality of molten salt corrosion behaviour of Ni-based alloys in molten fluoride salts. Furthermore, one can infer that the microstructural characteristics such as grain size, texture and dislocation density (not included in the present model) play a secondary role in the molten salt corrosion behaviour of Ni-based alloys [41].

Fig. 10 presents the contribution of individual alloying elements to the overall mass loss of tested alloys. The figure clearly shows that the depletion of Cr makes the largest contribution to mass loss in all tested alloys exposed to molten salt corrosion. This is in agreement with previous studies, which pointed out the importance of Cr on molten salt corrosion [30,33,42]. Hence, the high Cr content in the ODS MA754® alloy is the main reason for its poorer molten salt corrosion performance in comparison to GH3535 and HASTELLOY-N® alloy. The current results further suggests that the amount of depletion an alloying element undergoes is proportional to its diffusion coefficient and its content within the alloy. That is, the higher content alloying elements will exhibit more depletion than other lower content alloying elements even if their ΔG_f^o are similar (e.g. Cr and Mn). If content and ΔG_f^o are both similar, the alloying element with the larger diffusion coefficient will exhibit more depletion (e.g. Mn and Si). Finally, whilst the presence of nano-sized Y_2O_3 particles have a negative effect on the corrosion performance of MA754® alloy as outlined in Eq. 13–15, its effect on the overall corrosion performance of the alloy appears to be negligible compared to the effect of Cr depletion.

The numerical model results show that for similar Ni-based alloys exposed to FLiNaK molten salt, each alloying element's contribution to overall mass loss through molten salt corrosion can be approximated if that alloying element's diffusion constant and content are known, and to maximise molten salt corrosion resistance, the content and diffusion coefficient of depletion-prone alloying elements should be minimised. Whilst the diffusion constant of an alloying element cannot be significantly altered without a dramatic change in alloy composition and/or microstructure, the molten salt corrosion resistance of a Ni-based alloy may be improved by reducing or minimising the content of alloying elements more thermodynamically prone to depletion without significantly impacting other important alloy properties [42]. In practice, this effect has demonstrated experimentally in numerous studies. For example, in the original MSRE, researchers compared alloys containing less than 8 wt.% Cr with alloys containing more than 15 wt.% Cr and found that alloys with a lower Cr content exhibited significantly higher molten salt corrosion resistance while retaining a high oxidation resistance [30,43].

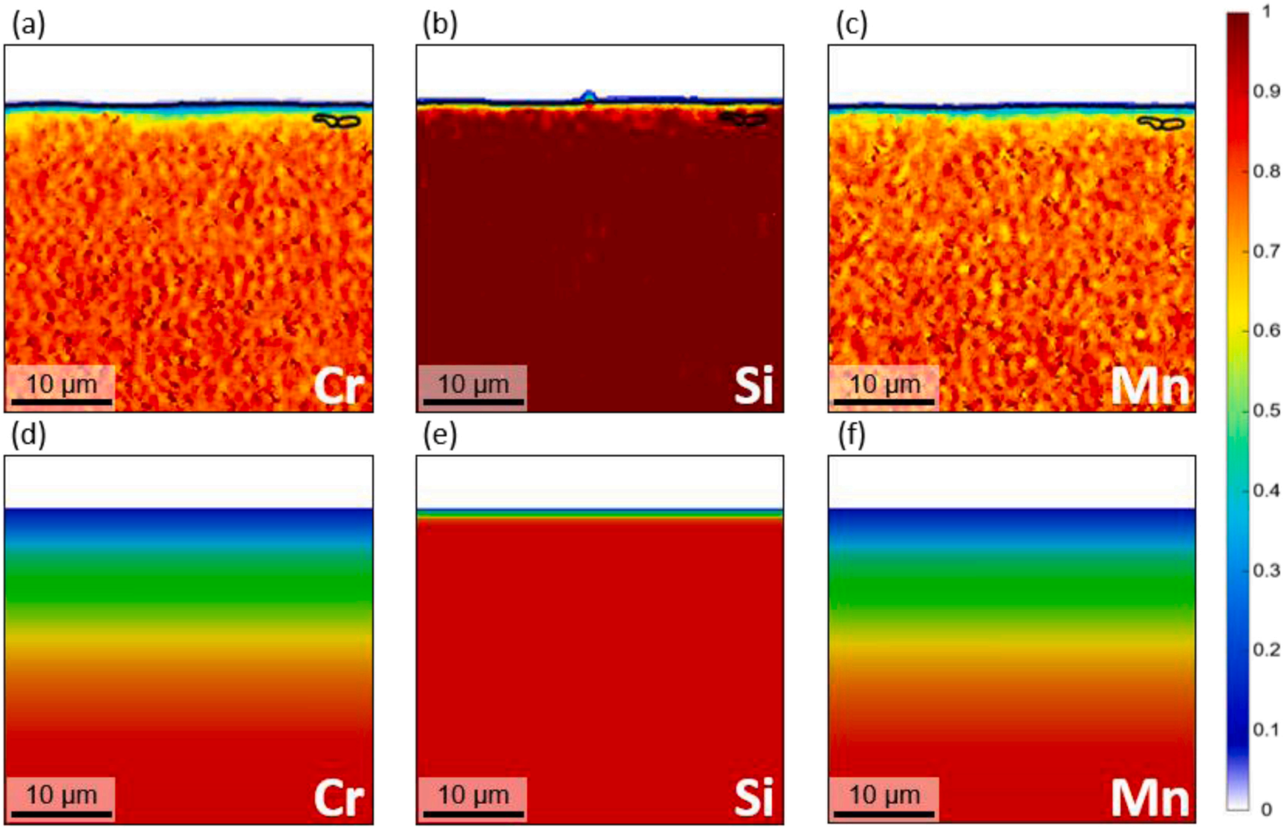

Fig. 9. EDS maps and modelled corrosion profiles taken at 2000× magnification of HASTELLOY-N® following molten salt corrosion tests at 750 °C for 300 h, showing (a) Cr EDS map; (b) Mn EDS map; (c) Si EDS map; (d) Cr modelled corrosion profile; (e) Mn modelled corrosion profile and (f) Si modelled corrosion profile. Figures (a)-(f) are min-max normalised between 0-1 (see scale bar).

Finally, it is noted that the numerical model can only predict the contribution of bulk diffusion to an alloy's overall mass loss, and thus any factors that can affect corrosion behaviour outside of bulk diffusion will affect the accuracy of the model. For example, factors such as alloy microstructure, operating temperature, concentration of impurities in the molten salt mixture, corrosion testing time and corrosion testing crucible material can all meaningfully affect experimental corrosion testing results without affecting the numerical model's predicted mass loss. While the model is a useful predictive tool, variations between underestimating or overestimating the degree of corrosion for different alloy compositions in comparison to experimental results suggests that the model requires future refinement.

4. Conclusions

In the present work we compared the molten salt corrosion performance of Y_2O_3-strengthened MA754® alloy with Ni-Mo-Cr HASTELLOY-N® and GH3535 alloys. Unlike GH3535 and HASTELLOY-N®, the MA754® was not developed with molten salt corrosion resistance in mind, however, it exhibits excellent high-temperature strength, creep, and creep-fatigue properties, which are known to limit the use of GH3535 and HASTELLOY-N® at high temperatures above 750 °C. The obtained results show that the corrosion performance of the MA754® alloy is significantly worse when compared to purpose-developed molten-salt-facing Ni-Mo-Cr alloys. MA754® exhibited approximately 80 % increase in material mass loss compared to GH3535 and HASTELLOY-N® after exposure to FLiNaK molten salt at 750 °C for 300 h. We show, based on experimental results and numerical simulations, that the enhanced corrosion of MA754® can be attributed to the significantly higher Cr content (20 wt.%) of the alloy compared to GH3535 and HASTELLOY-N® (7–7.5 wt.%). The current results, however, suggest that the presence of Y_2O_3 dispersions, which are known to significantly improve the high temperature properties of the alloy, play only a minor role in its molten salt corrosion performance. It is thus believed that the obtained results open doors to the development of low Cr content ODS alloys for molten salt applications in the temperature range above 750 °C where the conventional alloys fail to meet the requirements. These alloys would exhibit excellent high-temperature properties (similar to MA754®) while also providing good molten salt corrosion resistance (similar to GH3535 and HASTELLOY-N®).

Author statement

Ming Lee: Formal analysis, Visualization, Writing - Original Draft Ondrej Muránsky: Conceptualization, Methodology, Investigation, Supervision, Writing - Original Draft. Inna Karatchevtseva: Investigation, Methodology. Hefei Huang: Resources, Writing - Review & Editing. Kevin Laws: Supervision, Writing - Review & Editing.

Declaration of Competing Interest

The authors report no declarations of interest.

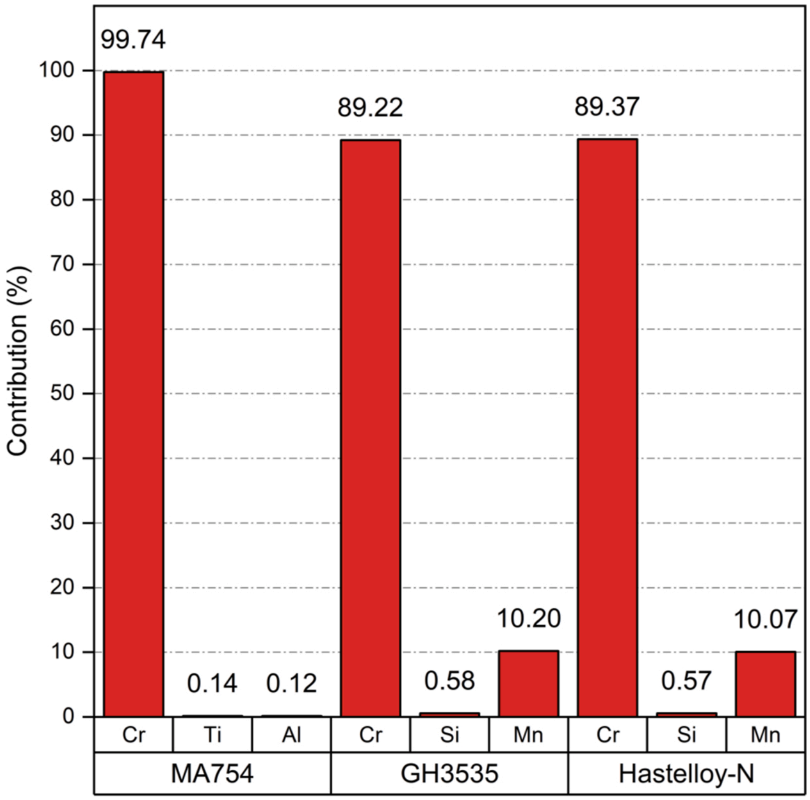

Fig. 10. Contribution (%) of modelled alloying elements the overall mass loss of Inconel MA754®, GH3535 and HASTELLOY-N® following molten salt corrosion tests at 750 °C for 300 h.

Acknowledgement

The authors would like to thank Mr Tim Palmer, from the Metallography Lab at ANSTO, for the preparation of test specimens. This research was funded by ANSTO's internal research funding.

Appendix A1 Theoretical maximum concentration of impurities in FLiNaK molten salt prepared for corrosion testing based on supplier specifications. FLiNaK molten salt was prepared by mixing commercially available LiF (62497), NaF (201154) and KF (60239) supplied by Sigma-Aldrich, at eutectic composition (46.5—11.5—42 mol%)

Impurity	i_i (ppm)			i_{FLiNaK}(mg/200 g)			Total (mg/200 g)	Total (ppm)
	LiF	NaF	KF	LiF	NaF	KF		
Ag	–	–	5	–	–	0.591	0.591	2.96
Al	200	–	5	11.7	–	0.591	12.3	61.4
As	5	–	–	0.292	–	–	0.292	1.46
Ba	50	–	5	2.92	–	0.591	3.51	17.6
Bi	20	–	5	1.17	–	0.591	1.76	8.80
Ca	500	–	10	29.2	–	1.18	30.4	152
Cd	5	–	5	0.292	–	0.591	0.883	4.42
Co	5	–	5	0.292	–	0.591	0.883	4.42
Cr	10	–	5	0.584	–	0.591	1.18	5.88
Cu	50	–	5	2.92	–	0.591	3.51	17.6
Fe	50	30	5	2.92	0.702	0.591	4.21	21.1
K	100	200	–	5.84	4.68	–	10.5	52.6
Li	–	–	5	–	–	0.591	0.591	2.96
Mg	100	–	5	5.84	–	0.591	6.43	32.2
Mn	5	–	5	0.292	–	0.591	0.883	4.42
Mo	5	–	5	0.292	–	0.591	0.883	4.42
Na	500	–	5000	29.2	–	591	620	3100
Ni	100	–	5	5.84	–	0.591	6.43	32.2
Pb	10	30	5	0.584	0.702	0.591	1.88	9.39
Sr	100	–	5	5.84	–	0.591	6.43	32.2
Tl	–	–	5	–	–	0.591	0.591	2.96
Zn	10	–	5	0.584	–	0.591	1.18	5.88
Cl^{-}	100	50	50	5.84	1.17	5.91	12.9	64.6
SO_3^{2-}	–	50	–	–	1.17	–	1.17	5.85
SO_4^{2-}	500	300	100	29.2	7.02	11.8	48.0	240

Appendix A2 Gibbs free energy of formation (ΔG_f^o) of FLiNaK constituent salts and potential corrosion products, per mol of F_2, evaluated at 750 °C

Fluoride	Formation equation	$\nu_{i,p}\Delta G_f^{o}$ (kJ/mol)	$\nu_{F,r}$	ΔG_f^{o} (kJ/mol F_2)
LiF(l)	$2Li(s)+F_2(g)\rightarrow 2LiF(l)$	2(-515.68)	1	−1031.4
NaF(l)	$2Na(s)+F_2(g)\rightarrow 2NaF(l)$	2(-462.63)	1	−925.26
KF(l)	$2K(s)+F_2(g)\rightarrow 2KF(l)$	2(-460.97)	1	−921.95
AlF_3(l)	$2Al(s)+3F_2(g)\rightarrow 2AlF_3(l)$	2(-1190.2)	3	−793.49
CoF_2(l)	$Co(s)+F_2(g)\rightarrow CoF_2(l)$	1(-510.54)	1	−510.54
CoF_3(l)	$2Co(s)+3F_2(g)\rightarrow 2CoF_3(l)$	2(-555.44)	3	−370.29
CrF_2(l)	$Cr(s)+F_2(g)\rightarrow CrF_2(l)$	1(-646.08)	1	−646.08
CrF_3(l)	$2Cr(s)+3F_2(g)\rightarrow 2CrF_3(l)$	2(-938.46)	3	−625.64
CuF_2(l)	$Cu(s)+F_2(g)\rightarrow CuF_2(l)$	1(-381.24)	1	−381.24
FeF_2(l)	$Fe(s)+F_2(g)\rightarrow FeF_2(l)$	1(-552.49)	1	−552.49
FeF_3(l)	$2Fe(s)+3F_2(g)\rightarrow 2FeF_3(l)$	2(-812.55)	3	−541.70
MnF_2(l)	$Mn(s)+F_2(g)\rightarrow MnF_2(l)$	1(-715.59)	1	−715.59
MoF_4(g)	$Mo(s)+2F_2(g)\rightarrow MoF_4(g)$	1(-840.98)	2	−420.49
MoF_5(g)	$2Mo(s)+5F_2(g)\rightarrow 2MoF_5(g)$	2(-1053.4)	5	−421.36
MoF_6(g)	$Mo(s)+3F_2(g)\rightarrow MoF_6(g)$	1(-1270.1)	3	−423.37
NiF_2(l)	$Ni(s)+F_2(g)\rightarrow NiF_2(l)$	1(-497.51)	1	−497.51
SiF_2(g)	$Si(s)+F_2(g)\rightarrow SiF_2(g)$	1(620.06)	1	−620.06
SiF_4(g)	$Si(s)+2F_2(g)\rightarrow SiF_4(g)$	1(1468.1)	2	−734.07
TiF_2(g)	$Ti(s)+F_2(g)\rightarrow TiF_2(l)$	1(-708.81)	1	−708.81
TiF_3(g)	$2Ti(s)+3F_2(g)\rightarrow 2TiF_3(g)$	2(-1142.7)	3	−794.86
WF_6(g)	$W(s)+3F_2(g)\rightarrow WF_6(g)$	1(-1420.10)	3	−473.36

References

[1] O. Edenhofer, R. Pichs-Madruga, Y. Sokona, J.C. Minx, E. Farahani, S. Kadner, K. Seyboth, A. Adler, I. Baum, S. Brunner, P. Eickemeier, B. Kriemann, J. Savolainen, S. Schlömer, C. von Stechow, T. Zwickel, Climate Change 2014 | Mitigation of Climate Change, Cambridge University Press, 2014.

[2] W. Ren, Considerations of Alloy N code extension for commercial molten salt reactor development and deployment, Pressure Vessels and Piping Conference (2018).

[3] H. Zhu, B. Li, M. Chen, C. Qiu, Z. Tang, Improvement of corrosion resistance of Hastelloy-N alloy in LiF-NaF-KF molten salt by laser cladding pure metallic coatings, Coatings 8 (2018) 322.

[4] H.G. MacPherson, The molten salt reactor adventure, Nucl. Sci. Eng. 90 (4) (1985) 374–380.

[5] J. Serp, M. ALlibert, O. Beneš, S. Delpech, O. Feynberg, V. Ghetta, D. Heuer, D. Holcomb, V. Ignatiev, J.L. Kloosterman, L. Luzzi, E. Merle-Lucotte, J. Uhlíř, R. Yoshioka, D. Zhimin, The molten salt reactor (MSR) in generation IV: overview and perspectives, Prog. Nucl. Energy 77 (2014) 308–319.

[6] E. González-Roubaud, D. Pérez-Osorio, C. Prieto, Review of commercial thermal energy storage in concentrated solar power plants: Steam vs. molten salts, Renew. Sustain. Energy Rev. 80 (2017) 133–148.

[7] S. Guillot, A. Faik, A. Rakhmatullin, J. Lambert, E. Veron, P. Echegut, C. Bessada, N. Calvet, X. Py, Corrosion effects between molten salts and thermal storage material for concentrated solar power plants, Appl. Energy 94 (2012) 174–181.

[8] A.K. Misra, J.D. Whittenberger, Fluoride salts and container materials for thermal energy storage applications in the temperature range 973-1400 K, 22nd Intersociety Energy Conversion Engineering Conference (1987).

[9] O. Muránsky, C. Yang, H. Zhu, I. Karatchevtseva, P. Sláma, Z. Nový, L. Edwards, Molten salt corrosion of Ni-Mo-Cr candidate structural materials for Molten Salt Reactor (MSR) systems, Corros. Sci. 159 (2019).

[10] L. Jiang, C. Fu, B. Leng, Y. Jia, X. Ye, W. Zhang, Q. Bai, S. Xia, Z. Li, F. Liu, X. Zhou, Influence of grain size on tellurium corrosion behaviors of GH3535 alloy, Corros. Sci. 148 (2019) 110–122.

[11] Z. Novy, J. Džugan, P. Wangyao, L. Kraus, Development of forming processes for MoNiCr alloy, Key Eng. Mater. 658 (2015) 3–7.

[12] T.C. Totemeier, T.M. Lillo, J.A. Simpson, Elevated temperature strength of fine-grained INCONEL alloy MA754, Metall. Mater. Trans. 36 (2005) 2552–2555.

[13] D. Bhattacharyya, J. Davis, M. Drew, R.P. Harrison, L. Edwards, Characterization of complex carbide–silicide precipitates in a Ni–Cr–Mo–Fe–Si alloy modified by welding, Mater. Characterisation 105 (2015) 118–128.

[14] P. Shahinian, K. Sadananda, Fatigue and creep crack growth in oxide dispersion strengthened INCONEL MA-754, Metall. Trans. A 21 (1990) 177–187.

[15] C. Yen, T.E. Howson, F. Cosandey, J.K. Tien, Creep fracture processes of oxide dispersion strengthened mechanically alloyed inconel alloy ma 754, Metall. Trans. A 14 (1983) 1232.

[16] J.J. Stephens, W.D. Nix, The effect of grain morphology on longitudinal creep properties of INCONEL MA 754 at elevated temperatures, Metall. Trans. A 16 (1985) 1307–1324.

[17] A.H. Rosenstein, J.K. Tien, W.D. Nix, Void formation in INCONEL MA-754 by high temperature oxidation, Metall. Trans. A 17 (1986) 151–162.

[18] Y. Zhu, J. Qiu, J. Hou, W. Liu, H. Chen, H. Ai, G. Yu, J. Wang, X. Zhou, Effects of SO42- ions on the corrosion of GH3535 weld joint in FLiNaK, J. Nucl. Mater. 492 (2017) 122–127.

[19] F. Ouyang, C. Chang, B. Yo, T. Yeh, J. Kai, Effect of moisture on corrosion of Ni-based alloys in molten alkali fluoride FLiNaK salt environments, J. Nucl. Mater. 437 (1–3) (2013) 201–207.

[20] “MATLAB - MathWorks - MATLAB & Simulink,” MathWorks, 2020 [Online]. Available: https://au.mathworks.com/products/matlab.html.

[21] R. Hielscher, D. Mainprice, F. Bachmann, R. Kilian, F. Bartel, O.K. Johnson, B. E. Sørensen, MTEX Toolbox | MTEX [Online]. Available:, 2020 https://mtex-toolbox.github.io/.

[22] Abaqus Unified FEA - SIMULIA™ by Dassault Systèmes®, Dassault Systèmes, 2020 [Online]. Available: https://www.3ds.com/products-services/simulia/products/abaqus/.

[23] J.W. Evans, K.T. Lee, Accelerated testing and data analysis. Product Integrity and Reliability in Design, Springer, 2001, pp. 312–337.

[24] H. Cheng, F. Han, Y. Jia, Z. Li, X. Zhou, Effects of Te on intergranular embrittlement of a Ni–16Mo–7Cr alloy, J. Nucl. Mater. 461 (2015) 122–128.

[25] X. Chu, H. Cheng, C. Fu, B. Leng, Y. Jia, F. Liu, Z. Li, Effect of thermal exposure time on tellurium-induced embrittlement of Ni–16Mo–7Cr–4Fe alloy, Nucl. Sci. Tech. 28 (12) (2017) 1–6.

[26] Y. Zhu, J. Hou, G. Yu, J. Qiu, S. Chen, X. Zhou, Effects of exposing temperature on corrosion performance of weld joint of a Ni–Mo–Cr alloy, J. Fluor. Chem. 182 (2016) 69–75.

[27] Samuel W. McAlpine, Natasha C. Skowronski, Weiyue Zhou, Guiqiu (Tony) Zheng, Michael P. Short, Corrosion of commercial alloys in FLiNaK molten salt containing EuF3 and simulant fission product additives, J. Nuclear Mater. 532 (2020).

[28] A.E. Danon, O. Muránsky, I. Karatchevtseva, Z. Zhang, Z.J. Li, N. Scales, J. J. Kruzic, L. Edwards, Molten salt corrosion (FLiNaK) of a Ni–Mo–Cr alloy and its welds for application in energy-generation and energy-storage systems, Corros. Sci. 164 (March) (2020).

[29] Luke C. Olson, James W. Ambrosek, Kumar Sridharan, Mark H. Anderson, Todd R. Allen, Materials corrosion in molten LiF–NaF–KF salt, J. Fluor. Chem. 130 (1) (2009) 67–73.

[30] K. Sridharan, T.R. Allen, Corrosion in molten salts. Molten Salts Chemistry, Elsevier, 2013, pp. 241–267.

[31] Y. Wang, S. Zhang, X. Ji, P. Wang, W. Li, Material corrosion in molten fluoride salts, Int. J. Electrochem. Sci. 13 (2018) 4891–4900.

[32] L.C. Olson, J.W. Ambrosek, K. Sridharan, M.H. Anderson, T.R. Allen, Materials corrosion in molten LiF–NaF–KF salt, J. Fluor. Chem. 130 (1) (2009) 67–73.

[33] C.S. Sona, B.D. Gajbhiye, P.V. Hule, A.W. Parwardhan, C.S. Mathpati, A. Borgohain, N.K. Maheshwari, High temperature corrosion studies in molten salt-FLiNaK, Corros. Eng. Sci. Technol. 49 (4) (2014) 287–295.

[34] J. Zhang, Impurities in primary coolant salt of FHRs: chemistry, impact, and removal methods, Energy Technol. 7 (2019).

[35] M.K.M.B.V. Pavlik, Corrosion behavior of Incoloy 800H/HT in the fluoride molten salt FLiNaK + MFx (MFx = CrF3, FeF2, FeF3 and NiF2), R. Soc. Chem. 39 (2015) 9841–9847.

[36] J. Hou, G. Yu, C. Zeng, H. Ai, R. Xie, Y. Chen, X. Zhou, L. Xie, J. Wang, Effects of exposing duration on corrosion performance in weld joint of Ni-Mo-Cr alloy in FLiNaK molten salt, J. Fluor. Chem. 191 (2016) 110–119.

[37] J. Qiu, B. Leng, H. Liu, D.D. Macdonald, A. Wu, Y. Jia, W. Xue, G. Yu, X. Zhou, Effect of SO42− on the corrosion of 316L stainless steel in molten FLiNaK salt, Corros. Sci. 144 (2018) 224–229.

[38] C. Yang, O. Muránsky, H. Zhu, I. Karatchevtseva, R. Holmes, M. Avdeev, Y. Jia, H. Huang, X. Zhou, Corrosion performance of Ni-16%wt.Mo-X%wt.SiC alloys in FLiNaK molten salt, Corros. Sci. 143 (2018) 240–248.

[39] T. Watanabe, M. Kondo, T. Nagasaka, A. Sagara, Corrosion characteristic of AlN, Y2O3, Er2O3 and Al2O3 in Flinak for molten salt blanket system, J. Plasma Fusion Res. SERIES 9 (2010) 342–347.

[40] S.H. Cho, J.M. Hur, C.S. Seo, J.S. Yoon, S.W. Park, Hot corrosion behavior of Ni-base alloys in a molten salt under an oxidizing atmosphere, J. Alloys. Compd. 468 (1–2) (2009) 263–269.

[41] O. Muránsky, I. Karatchevtseva, A.E. Danon, R. Holmes, P. Huai, Z. Zhang, Impact of dislocations and dislocation substructures on molten salt corrosion of alloys under plasticity-imparting conditions, Corros. Sci. 176 (2020).

[42] D.F. Williams, Corrosion issues in molten fluoride salts, American Nuclear Society Annual Conference (2006).

[43] J.H. DeVan, Effect of Alloying Additions on Corrosion Behavior of Nickel-Molybdenum Alloys in Fused Fluoride Mixtures, Oak Ridge National Laboratory, 1969.

[44] H.W. Allison, H. Samelson, Diffusion of aluminum, magnesium, silicon, and zirconium in nickel, J. Appl. Phys. 30 (1959) 1419–1424.

[45] S.P. Murarka, M.S. Anand, R.P. Agarwala, Diffusion of chromium in nickel, J. Appl. Phys. 35 (1964) 1339–1341.

[46] K. Hoshino, Y. Iijima, K. Hirano, Diffusion of vanadium, chromium, and manganese in copper, Metall. Trans. A 8 (1977) 469–472.

[47] R.A. Swalin, A. Martin, R. Olson, Diffusion of magnesium, silicon, and molybdenum in nickel, J. Miner. Metals Mater. Soc. 9 (1957) 936–939.

[48] S.V. Divinski, I. Stloukal, L. Kral, C. Herzig, Diffusion of titanium and nickel in B2 NiTi, Defect Diffus. Forum 289 (2009) 377–382.